

## Article

# Photocatalytic Degradation of Humic Acid Using Bentonite@Fe<sub>3</sub>O<sub>4</sub>@ZnO Magnetic Nanocomposite: An Investigation of the Characterization of the Photocatalyst, Degradation Pathway, and Modeling by Solver Plugin

Ayat Hossein Panahi <sup>1</sup>, Tariq J. Al-Musawi <sup>2,†</sup> , Mahdieh Masihpour <sup>3</sup>, Seyedeh Fatemeh Tabatabaei Fard <sup>4</sup> and Negin Nasseh <sup>5,6,\*,†</sup>

- <sup>1</sup> Student Research Committee, Department of Environmental Health Engineering, Hamadan University of Medical Sciences, Hamadan 6517838678, Iran  
<sup>2</sup> Building and Construction Techniques Engineering Department, Al-Mustaqbal University, Hillah 51001, Iraq  
<sup>3</sup> Master of Environmental Health Engineering, Department of Environmental Health, Semnan University of Medical Sciences, Semnan 3514799442, Iran  
<sup>4</sup> Environmental Health Engineering, Birjand University of Medical Sciences, Birjand 9717853577, Iran  
<sup>5</sup> Cellular and Molecular Research Center, Birjand University of Medical Sciences, Birjand 9717853577, Iran  
<sup>6</sup> Department of Health Promotion and Education, School of Health, Birjand University of Medical Sciences, Birjand 9717853577, Iran  
\* Correspondence: negin.nasseh2020@gmail.com  
† These authors contributed equally to this work.



**Citation:** Hossein Panahi, A.; Al-Musawi, T.J.; Masihpour, M.; Fard, S.F.T.; Nasseh, N. Photocatalytic Degradation of Humic Acid Using Bentonite@Fe<sub>3</sub>O<sub>4</sub>@ZnO Magnetic Nanocomposite: An Investigation of the Characterization of the Photocatalyst, Degradation Pathway, and Modeling by Solver Plugin. *Water* **2023**, *15*, 2931. <https://doi.org/10.3390/w15162931>

Academic Editors: Laura Bulgariu and Constantinos V. Chrysikopoulos

Received: 23 March 2023

Revised: 20 April 2023

Accepted: 27 April 2023

Published: 14 August 2023



**Copyright:** © 2023 by the authors. Licensee MDPI, Basel, Switzerland. This article is an open access article distributed under the terms and conditions of the Creative Commons Attribution (CC BY) license (<https://creativecommons.org/licenses/by/4.0/>).

**Abstract:** Humic acid (HA), the most highly prevalent type of natural organic matter (NOM), plays an effective role in the generation of disinfectant byproducts such as trihalomethanes and haloacetic acid, which are well known to be definitive carcinogens. Therefore, the proactive elimination of HA from water and wastewater is a crucial means of preventing this pollutant from reacting with the chlorine incorporated during the disinfection process. This study investigated the UV light photocatalytic elimination of HA, employing a bentonite@Fe<sub>3</sub>O<sub>4</sub>@ZnO (BNTN@Fe<sub>3</sub>O<sub>4</sub>@ZnO) magnetic nanocomposite. The most significant variables pertinent to the photocatalytic degradation process examined in this work included the pH (3–11), nanocomposite dose (0.005–0.1 g/L), reaction time (5–180 min), and HA concentration (2–15 mg/L). The synthesized materials were characterized via field emission scanning electron microscopy (FE-SEM), Fourier-transform infrared spectroscopy (FTIR), X-ray diffractometer (XRD), energy-dispersive X-ray spectroscopy (EDX), and vibrating-sample magnetometer (VSM) techniques, all of which revealed outstanding catalytic properties for the BNTN@Fe<sub>3</sub>O<sub>4</sub>@ZnO. The conditions under which greater efficiency was achieved included a pH of 3, a nanocomposite dose of 0.01 g/L, and an HA concentration of 10 mg/L. Under these conditions, in just 90 min of photocatalytic reaction, an HA degradation efficiency of 100% was achieved. From the modeling study of the kinetic data, the Langmuir–Hinshelwood model showed good compliance ( $R^2 = 0.97$ ) with the empirical data and predicted values. Thus, it can be concluded that the BNTN@Fe<sub>3</sub>O<sub>4</sub>@ZnO catalyst acts very efficiently in the HA removal process under a variety of treatment conditions.

**Keywords:** bentonite@Fe<sub>3</sub>O<sub>4</sub>@ZnO; magnetic nanocomposite; humic acid; photocatalytic process; degradation pathway; modeling

## 1. Introduction

The rapid improvement of industrialization has resulted in the production and accumulation of numerous chemical wastes in aqueous environments worldwide [1–3]. Humic substances refer to a mixture of natural organic compounds regarded as the most significant compounds in environmental waters [4]. Depending upon their solubility in acidic

or alkaline conditions in aqueous solutions, these humic substances are categorized as hymine, *HA*, and fulvic acid (FA), according to Zhan et al. 2010 [5]. When they are present in concentrations exceeding 5 mg/L, these compounds cause the water color to turn yellow or brown [6]. In natural water sources with pH levels above 2, the humic substances in a solution carrying a negative charge can be found in the concentration range of 20 to 30 mg/L [7]. Classified as dissolved organic carbon (DOC), these compounds (*HAs*) are limited to the surface water, and normally compose roughly 70% of the DOC [8]. The decomposition of plant and animal species comprises one of the main constituents of *HAs* [9]. As natural organic polyelectrolytes, *HAs* account for the greatest proportion of naturally soluble organic matter in aqueous bodies [10]. The *HA* present in aqueous systems induces a negative effect on both the appearance and taste of the water. The *HA* is capable of reacting with the chloride added to the drinking water treatment systems to generate disinfectant byproducts such as trihalomethanes (THMs) and haloacetic acid, which can endanger human health [11,12].

According to the norms of the World Health Organization (WHO), the maximum permissible quantity of trihalomethane is 100 micrograms per liter of drinking water, while the US Environmental Protection Agency cites the maximum permissible level of trihalomethane as 40 micrograms per liter of drinking water and the maximum permissible level of haloacetic acids as 30 micrograms per liter of drinking water [13]. In several epidemiological works, the ill effects of trihalomethanes and haloacetic acids on human health are reported, which include acute reproductive effects, toxicity, carcinogenicity and mutagenicity, bladder and colon cancer, adverse effects on birth, and a decrease in neonatal growth. Further, when these macromolecular organic materials are present, the purification processes can become disturbed by their porous membranes or fine porous adsorbents [14,15].

To enable the elimination of *HA* from aqueous solutions, several techniques have been investigated, such as photo-Fenton [16] and photocatalytic [17] processes, activated carbon [18], and electrocoagulation [19]. At present, advanced oxidation processes (AOPs) take the spotlight as they are very efficient, provide a high degradation rate, and possess the capacity to remove all hazardous and non-biodegradable compounds, producing fewer byproducts [20]. During the process, AOPs release active free radicals which are then used in the decomposition of non-degradable organic matter [21]. Photocatalysis is the most popular method among various AOPs as a means of eliminating hazardous waste, particularly because it can break organic compounds down into substances that have a lower toxicity or cause less harm [22]. Photolytic and photocatalytic processes are strategies that demonstrate promise in the elimination of organic substances and other emerging organic pollutants [23]. Recently, metal oxide semiconductors have demonstrated strong photocatalytic capacities in the decomposition of harmful organic matter to low-risk molecules under light irradiation [24]. In recent times, the photocatalysis process has ranked high among the most extensively applied AOPs for the degradation of organic matter. Normally, the photocatalytic method involves the use of a semiconductor material (ZnO and TiO<sub>2</sub> nanoparticles) and a beam source (sunlight, simulated sunlight, and UV) and causes the generation of free radicals [25]. Semiconductor materials are significant and crucial as photocatalytic agents because in their chemical composition, the electronic structure of a metal atom possesses a characteristic valence band and an empty conduction band. The most discovered n-type semiconductors are ZnO semiconductors, which have a direct broadband gap ( $E_g = 3.37$  eV) that results from their intense electron–hole connection energy (60 MV), high mechanical temperature, strong stability, and piezoelectricity [26,27].

Natural clays such as bentonite demonstrate good catalytic properties, including a large surface area, excellent mechanical properties, acid and alkali resistance, high thermal stability, and various other suitable properties that can be explained by their unique structure. In addition, bentonite is a low-cost material [28,29]. Thus, bentonite is preferred for its use as a catalyst in AOPs [30].

Semiconductor catalysts such as  $\text{TiO}_2$ ,  $\text{ZrO}_2$ ,  $\text{WO}_3$ ,  $\text{ZnO}$ , and  $\text{ZnS}$  have found extensive use in photocatalytic reactions [31]. Among photocatalysts,  $\text{ZnO}$  shows the greatest photocatalytic activity as it is excitable at room temperature by itself under a wide range of optical irradiations. It should be noted that although  $\text{ZnO}$  and  $\text{TiO}_2$  semiconductors have very close band gap values,  $\text{ZnO}$  is capable of absorbing a larger portion of the UV spectrum compared to  $\text{TiO}_2$  [32]. It also has other advantages, such as its non-toxicity, high abundance, and availability. Homogeneous photocatalytic processes encounter issues with recoverability and reusability because centrifugation, which is a costly technique, is required to reuse the materials. This problem can be circumvented as magnetic properties can be induced into the material of the photocatalyst; this is one of the best and most efficient methods for the recovery of materials from the homogeneous phase [33] [34]. Some works have recently reported the use of iron-based compounds as a magnetic core to induce magnetic properties in photocatalysts [35]. Further, a middle layer can be used to stop the iron compounds from entering the reactor due to the recurrent utilization and degradation of the photocatalytic shell [36].

Based on a survey of the literature, we found that few studies have discussed the removal of humic acid compounds from aqueous solutions using a photocatalytic process. Keeping in mind that humic acid compounds are harmful and toxic substances that can harmfully affect different sectors of the life cycle, the removal of said hazardous compounds from wastewater is urgently needed to prevent their accumulation in the ecosystem. Therefore, the objective of this study was the synthesis of a bentonite@ $\text{Fe}_3\text{O}_4$ @ $\text{ZnO}$  (BNTN@ $\text{Fe}_3\text{O}_4$ @ $\text{ZnO}$ ) magnetic nanocomposite for the elimination of *HA* from aqueous solutions through photocatalysis.

## 2. Materials and Method

### 2.1. Chemicals and Instruments

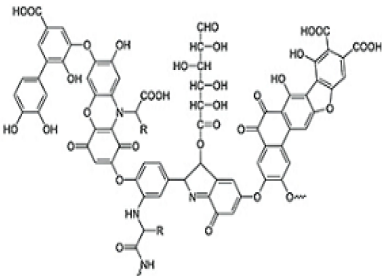
In the present investigation, *HA* was supplied by the Sigma Aldrich Company (St. Louis, MI, USA). Once the *HA* stock solution was prepared (1000 mg/L), it was stored at a temperature below 4 °C. Samples were then prepared from the stock solution via dilution. The chemical structure and other characteristics of the *HA* are listed in Table 1. The other reagents, namely, polyethylene glycol (PEG;  $\text{C}^{2n}\text{H}^{4n+2}\text{O}^{n+1}$ ), iron (III) chloride ( $\text{FeCl}_2 \cdot 4\text{H}_2\text{O}$ ), dimethyl formamide (DMF;  $\text{C}_3\text{H}_7\text{NO}$ ), nickel (II) chloride ( $\text{NiCl}_2 \cdot 6\text{H}_2\text{O}$ ), hydrazine hydrate ( $\text{N}_2\text{H}_4 \cdot \text{H}_2\text{O}$ ), tetraethyl orthosilicate (TEOS;  $\text{SiC}_8\text{H}_{20}\text{O}_4$ ), zinc nitrate ( $\text{ZnNO}_3 \cdot 6\text{H}_2\text{O}$ ), ammonia ( $\text{NH}_3$ ), hydrochloric acid (HCl), and sodium hydroxide (NaCl), were supplied by Merck Company. The residual concentration of the *HA* was evaluated via a UV/Vis spectrophotometer (CT06484 model). The UV radiation was provided by a PHILIPS PL-L TUV Lamp at a wavelength of 254 nm and a radiation intensity of 2500  $\mu\text{W}/\text{cm}^2$ . The synthesized magnetic nanocomposite (which included particle size, structure, and morphology), was characterized using Fourier-transform infrared spectroscopy (FT-IR; model: AVATAR, 370, Thermo Nicolet Company, USA), field emission scanning electron microscopy (FE-SEM; model: Zeiss-SIGMA VP-500, Germany), X-ray diffraction (XRD; model: X, Pert Pro, Panalytical Company, Malvern, UK), vibrating-sample magnetometry (VSM; model: 7400, Lakeshore Company, Carson, CA, USA), energy-dispersive X-ray spectroscopy (EDX; model: Zeiss-SIGMA VP-500, Germany), and diffuse reflectance spectroscopy (DRS; model: TEC-2048-Avaspec-A, Netherlands).

### 2.2. Synthesis of BNTN@ $\text{Fe}_3\text{O}_4$ @ $\text{ZnO}$ Magnetic Nanocomposite

The required BNTN was acquired from Avaj Mine, in the Qazvin province of Iran. First, it was ground using a pounder and then washed. Next, the BNTN was passed through a sieve with a mesh size of less than 100  $\mu\text{m}$  to obtain fine particles. The magnetic properties were induced through the following steps: first, 6 g of BNTN and 1.5 M NaCl were taken in a graduated flask and shaken at 300 rpm for 30 min. Next, 100 mL of distilled water was added into a double-neck flask and heated to 65 °C by a magnetic heater for half an hour; simultaneously, nitrogen gas was injected into it. Then, 1 g of  $\text{Fe}^{2+}$  and 2 g of  $\text{Fe}^{3+}$  salts were

poured into the double-neck flask placed on the magnetic heater. The supernatant thus obtained was then added to a volumetric flask containing 6 g of BNTN and 1.5 M NaCl. This mixture was subjected to stirring for 1 h. Next, the produced sediment was washed using distilled water and immediately dried. Then, 0.5 g of the acquired powder was dispersed in 50 mL of DMF and kept directly beneath the UV bath. Next, 0.6 g of  $\text{ZnONO}_3 \cdot 6\text{H}_2\text{O}$  was dissolved in 50 mL of DMF, and this was poured into the solution mentioned above. The suspension thus obtained was subjected to mixing with a mechanical shaker. Finally, 0.02 M NaOH was added and, employing a mechanical shaker, it was slowly mixed for 6 h. Finally, the resultant particles were separated utilizing a magnet, and repeated washing was performed with distilled water and ethanol. Eventually, the particles were oven-dried at 60 °C for 6 h and then calcinated in a furnace at a temperature of 500 °C for 2 h.

**Table 1.** Physiochemical properties of HA.

Molecular Structure	pKa	Molar Mass	Chemical Structure
$\text{C}_{187}\text{H}_{186}\text{O}_{89}\text{N}_9\text{S}_1$	<2	227.17 g/mol	

### 2.3. Photocatalytic Tests

In the present research, HA degradation was examined through the synthesis of a magnetic nanocomposite. To assess and determine the optimal conditions, the impact exerted by all crucial variables on the photocatalytic degradation of the HA was studied. The variables included pH (i.e., 3, 5, 7, 9, and 11), photocatalyst dose (0.005, 0.01, 0.02, 0.03, 0.04, 0.05, and 0.1 g/L), HA concentration (i.e., 2, 5, 10, and 15 mg/L) and contact time (i.e., 5, 10, 15, 30, 60, and 90 min). A schematic representation of the photocatalytic reactor is shown in Figure 1. The HA residual concentration in the photocatalytic reactor was determined by evaluating its absorption at 260 nm. To study the adsorption–desorption reactions between the HA and BNTN@Fe<sub>3</sub>O<sub>4</sub>@ZnO magnetic nanocomposite, the container in which the HA and photocatalyst were present was maintained in darkness for 30 min before it was exposed to the UV beam. A cooling system was installed to maintain the liquid temperature inside the main tank at 24 ± 2 °C. Finally, the equation provided below was applied to assess the performance of the photocatalytic reactor in the HA removal process.

$$R = \frac{HA_1 - HA_2}{HA_1} \quad (1)$$

In this equation,  $R$ ,  $HA_1$ , and  $HA_2$  represent the efficiency (%) of HA elimination, the initial concentration of HA, and the residual concentration of HA, respectively.

### 2.4. Kinetic Study of HA Degradation

In the current paper, the Langmuir–Hinshelwood (L-H) expression, a method used to model reaction velocities, was adopted for modeling the empirical data. In the literature, this model was extensively employed to depict the kinetic degradation of organic materials such as HA. The L-H equation provided as [37]:

$$-\left(\frac{dC}{dt}\right) = -K_{obs} \times C \quad (2)$$

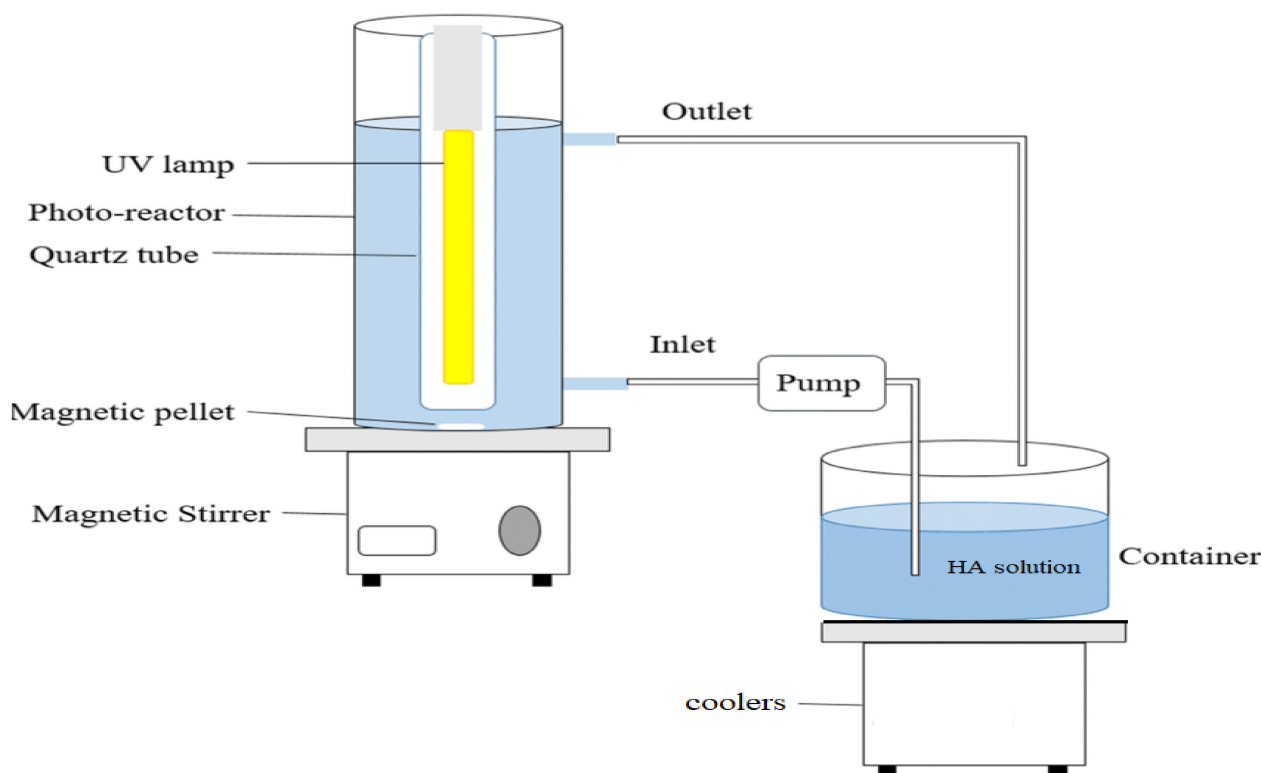


**Figure 1.** Schematic representation of the photocatalytic reactor.

Upon integrating Equation (2), it takes the following mathematical form,

$$\ln\left(\frac{C}{C_0}\right) = -K_{obs} \times t \quad (3)$$

In both equations (Equations (2) and (3)),  $K_{obs}$ ,  $C_0$ ,  $C$ , and  $t$  are the reaction constants of the pseudo-first-order (1/min), initial concentration of HA (mg/L), residual concentration of HA (mg/L), and contact time (min), respectively.

To model the degradation kinetics, the integrated rate law equation (Equation (3)), or  $(C = C_0 \times e^{-K_{obs} \times t})$ , is applied to ascertain the predicted values of the residual HA concentration post time  $t$ . Then, by referring to the chart of the predicted values versus the experimental values, the relationship between them was assessed by the determination of the coefficient ( $R^2$ ).

### 2.5. Reusability Tests

The reusability of the BNTN@Fe<sub>3</sub>O<sub>4</sub>@ZnO magnetic nanocomposite in HA degradation was assessed. It was found that 0.01 g/L of nanoparticles was able to be used four times for HA removal when conditions were optimal, and the quantity of non-reduction induced by the destruction of the photocatalyst was regarded as the percentage of reusability.

## 3. Results and Discussion

### 3.1. Study of Material Characterization

#### 3.1.1. XRD Analysis

The XRD spectrum of magnetic BNTN coated with zinc oxide is provided in Figure 2. The chief constituents of the BNTN employed in this work were calcite, illite, quartz, and albite. The base distance for the raw BNTN was observed to be 799.79 Å. Therefore, in  $2\theta$  equal to 21.47, 26.32, 28.01, 29.74, 35.33, 37.27, 39.92, 43.17, 46.61, 50.74, 60.19, and 67.74, peaks associated with BNTN are seen; further, in  $2\theta$  equal to 29.16, 35.73, 54.54, 56.19, 63.16, and 75.14, peaks are indicative of the presence of iron in the BNTN. The fact that

these crystal plates are linked to the inverted cubic spinel structure of the  $\text{Fe}_3\text{O}_4$  can be deduced based on the reference card number (ICSD 159976). In addition, the peaks related to zinc oxide are equal to 26.46, 28.13, 34.11, 37.16, 57.92, and 65.91. The synthesized nanocomposite was studied, and its size was estimated by applying the Scherrer equation in terms of the full width at half maximum (FWHM), and the most intense diffraction peak was visible at 34 nm.

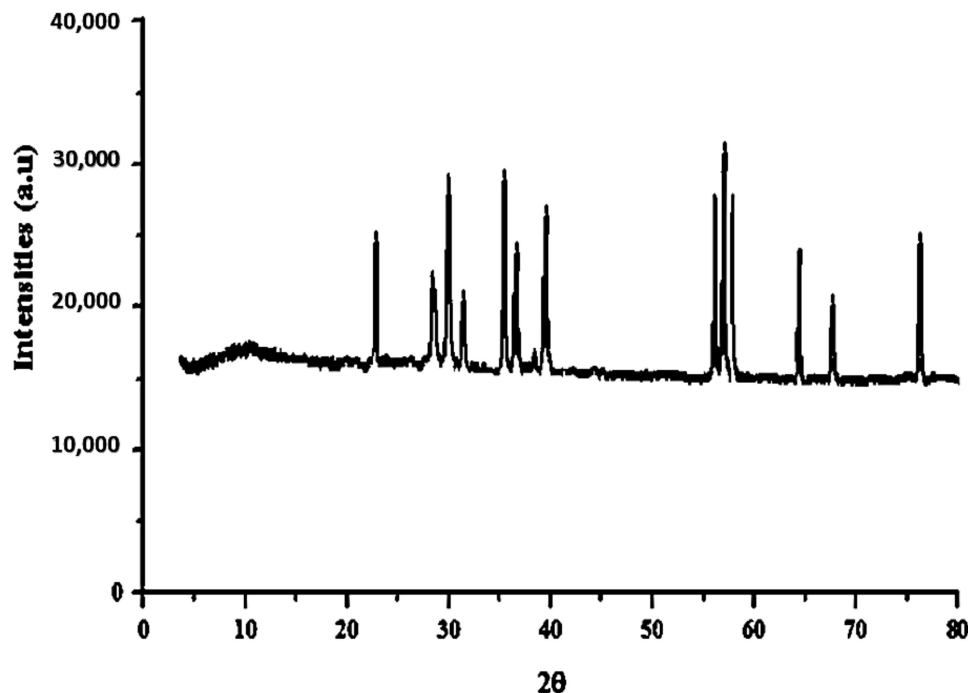


**Figure 2.** XRD graph of BNTN@ $\text{Fe}_3\text{O}_4$ @ZnO particles.

However, in the FESEM analyses, it could be recognized that the resulting nanoparticles have the propensity to accumulate because of their magnetic properties; therefore, their particle size is bigger than the value calculated from the Scherrer equation and is set at about 67 nm. This difference may arise because although the XRD analysis normally reveals the crystal size, the FESEM analysis shows the particle size. As a particle is composed of several crystals, this size can be justified. In the Scherrer formula,  $D$  represents the particle diameter,  $\beta$  is the peak width at half height,  $\theta$  indicates the diffraction angle at the peak location, and  $\lambda$  is the X-ray wavelength of the device ( $0.1540 \text{ nm} = \lambda$ ).

### 3.1.2. FTIR Analysis

The bands present in raw BNTN are seen at  $3401$ ,  $1643$ ,  $1489$ ,  $1028$ ,  $793$ ,  $690$ , and  $520 \text{ cm}^{-1}$ , as depicted in Figure 3. The broadband visible at  $3401 \text{ cm}^{-1}$  is accorded to the hydrogen bonds of the water molecules adsorbed onto the interlayer of the BNTN. The band observed at  $1643 \text{ cm}^{-1}$  is due to the flexural vibrations of the water molecules adsorbed onto the BNTN. The peak seen at  $1439 \text{ cm}^{-1}$  is caused by the bending vibrations of the C-H bonds. Further, the infrared spectrum in the BNTN shows a band at  $1028 \text{ cm}^{-1}$ , apparently due to the bending vibrations of the Si-O-Si. The quartz bands (Si-O) show proximity to  $790 \text{ cm}^{-1}$ . The band identified at  $520 \text{ cm}^{-1}$  is related to the bending vibrations of the O-Si-O. The  $690 \text{ cm}^{-1}$  band is also ascribed to the Al (Mg)-Si-O tetrahedral. The remaining peaks are evident from  $500$  to  $1000 \text{ cm}^{-1}$ ; however, they are likely produced by the functional groups, Fe-O-OH and Fe-O. In addition, the bands present at  $850$ ,  $1350$ ,  $1700$ , and  $2900 \text{ cm}^{-1}$  can also be related to the zinc oxide functional groups.

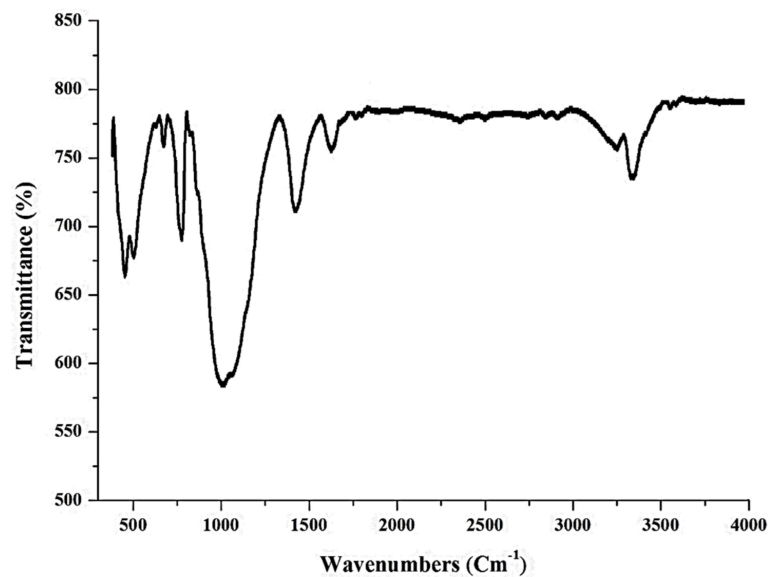


**Figure 3.** FT-IR graph of BNTN@Fe<sub>3</sub>O<sub>4</sub>@ZnO particles.

### 3.1.3. DRS Analysis

The optical properties of the composite employed in this work were subjected to DRS analysis for evaluation, as shown in Figure 4. Based on prior studies, the band gap was around 3.2 electron volts; however, from this analysis, the presence of other materials, such as BNTN and iron oxide, induced a slight alteration in the zinc oxide band, and the value is now 3.1 electron volts.

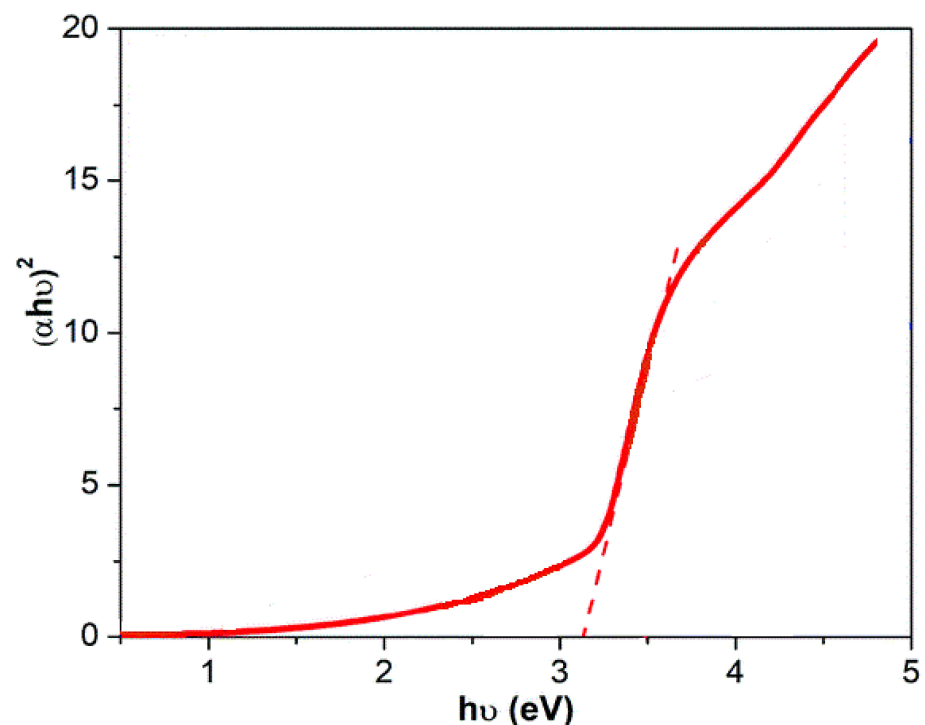


**Figure 4.** DRS spectra of BNTN@Fe<sub>3</sub>O<sub>4</sub>@ZnO particles.

### 3.1.4. FESEM Analysis

From Figure 5, the FESEM images of the BNTN, BNTN@Fe<sub>3</sub>O<sub>4</sub>, and BNTN@Fe<sub>3</sub>O<sub>4</sub>@ZnO particles are clear. Based on Figure 5A, the BNTN appears bulky, with a massive morphology and irregular flakes; the surface appears smooth, as is evident from Figure 5. In

addition, Figure 5B indicates that the iron particles are seated well and quite evenly on the BNTN. The final BNTN@Fe<sub>3</sub>O<sub>4</sub>@ZnO composite can be seen in Figure 5C. Obviously, the zinc oxide particles present on the magnetic BNTN are deposited in a layer that is thin and compacted.

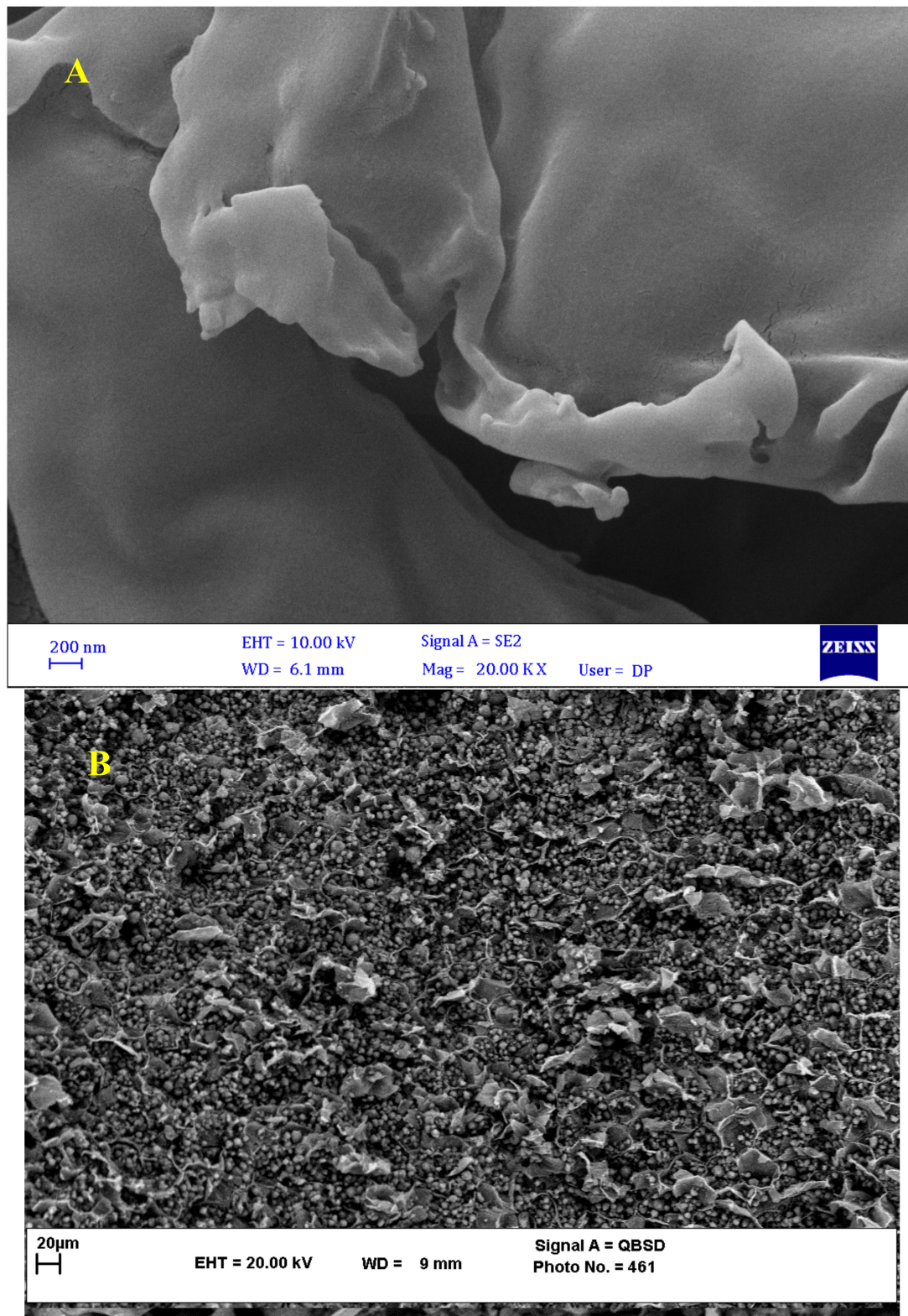
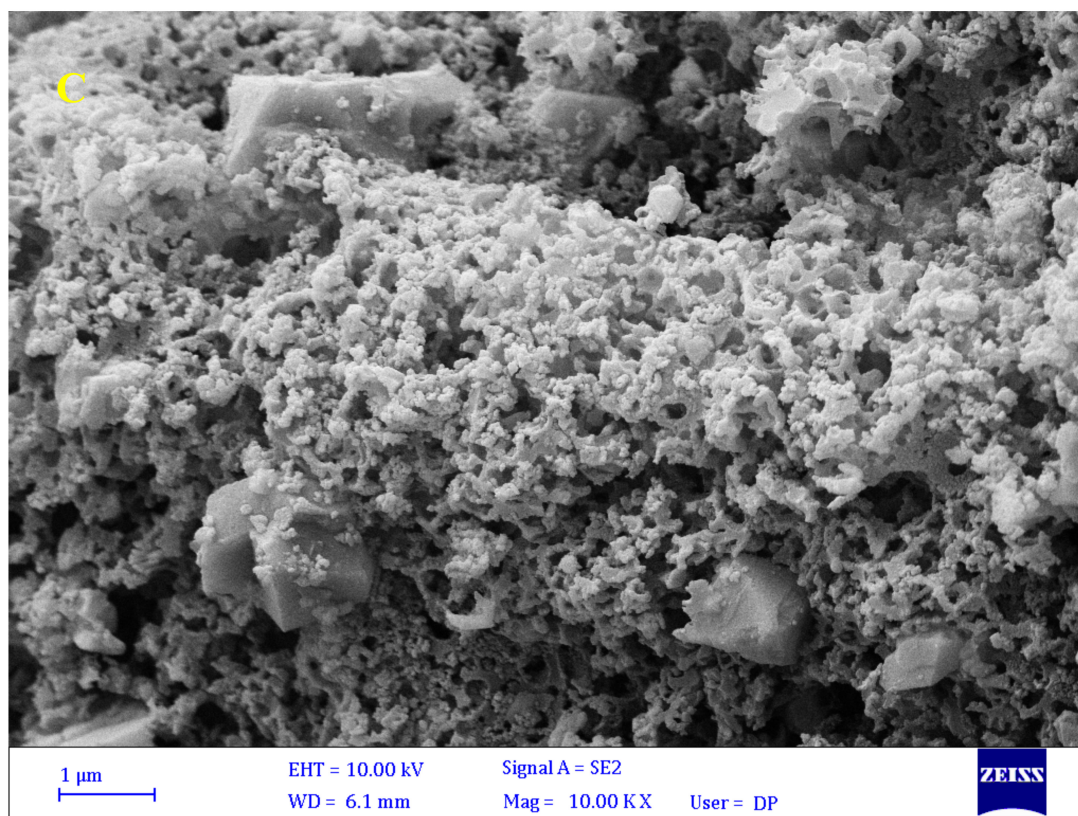


Figure 5. Cont.



**Figure 5.** FESEM spectra of BNTN (A), BNTN@Fe<sub>3</sub>O<sub>4</sub> (B), and BNTN@Fe<sub>3</sub>O<sub>4</sub>@ZnO (C) particles.

### 3.1.5. EDX Analysis

The abundance percentages of the elements in the BNTN@Fe<sub>3</sub>O<sub>4</sub>@ZnO nanocomposite used in this work are found in the EDX analysis provided in the authors' previous study. This image distinctly reveals that silica is present in the BNTN and comprises the highest weight percentage of the nanocomposite. The presence of iron also helps to explain the magnetic properties of the nanocomposite. However, as the outermost layer of the nanocomposite is oxidized, the image suggests that high weight percentages of zinc and oxygen can be easily achieved.

### 3.1.6. VSM Analysis

The VSM magnetometer was able to study the magnetic properties of the synthesized nanoparticles (magnetic BNTN coated with zinc oxide) through the vibrations of their samples at room temperature (Figure 6).

Depending upon the magnetization curve, it is evident that this material is supermagnetic, with a magnetic saturation of approximately 50. Thus, the conclusion is drawn that when the final nanocomposite employed in this work is dispersed in water, it can easily and quickly be gathered using an external magnetic field, and it is also easily dispersed in the solution via slight shaking.

## 3.2. Effect of Environmental Variables

The literature contains ample proof that environmental variations highly influence the efficiency of photocatalytic reactions. Hence, preliminary experiments were performed to estimate the effects of vital parameters such as the pH, photo-catalyst dose, HA concentration, and contact time on the efficiency of HA removal by the BNTN@Fe<sub>3</sub>O<sub>4</sub>@ZnO magnetic nanocomposite.

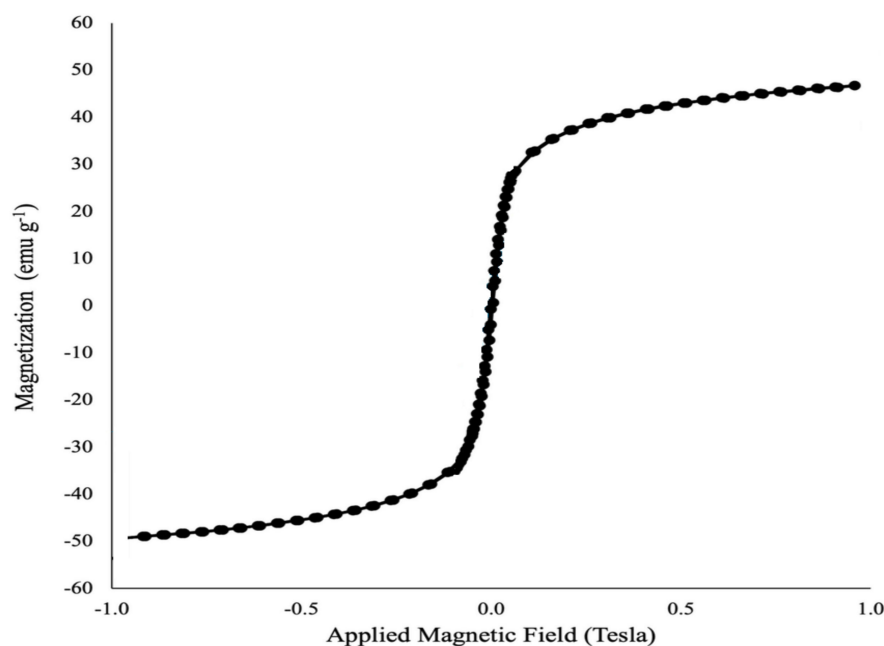


**Figure 6.** VSM spectra of BNTN@Fe<sub>3</sub>O<sub>4</sub>@ZnO particles.

### 3.2.1. Influence of pH

Among the critical variables in the photocatalytic reaction, the solution pH exerts the greatest effect on the efficiency of pollutant degradation. This is due to many reasons, the first being the ability of the pollutant molecules to dissolve in aqueous solutions, which is governed by the pH of the medium. This dissolubility is very different according to its pH value. *HA* is the fraction of humic material which remains insoluble in aqueous systems with  $\text{pH} < 2$ , though it dissolves at higher pH values. Hence, the conclusion is drawn that *HA* compounds carry negative charges on their surface when the  $\text{pH} > 2$ . Another significant situation in which pH can influence the process is when the pH reaches a zero point of charge ( $\text{pH}_{\text{zpc}}$ ). Hence, it is vital to ascertain the catalyst's surface charge before performing the photocatalytic tests. The findings of the  $\text{pH}_{\text{zpc}}$  determination test are shown in Figure 7B. This figure indicates that the  $\text{pH}_{\text{zpc}}$  of the BNTN@Fe<sub>3</sub>O<sub>4</sub>@ZnO magnetic nanocomposite is very close to 4.88 (dimensionless). Therefore, it can be concluded that the BNTN@Fe<sub>3</sub>O<sub>4</sub>@ZnO MNC surface can be saturated by negative charges derived from the excess OH<sup>−</sup> ions when the solution pH is higher than  $\text{pH}_{\text{zpc}}$ ; however, the photocatalyst surface will carry the positive charges from the H<sup>+</sup> protons when the solution pH drops to less than the  $\text{pH}_{\text{zpc}}$ . From the explanation cited above, an electrostatic force (attraction or repulsion) is created between the *HA* and the photocatalyst, which influences the *HA* degradation via photocatalysis.

In this work, an investigation into the photocatalytic degradation of *HA* at various pH values (i.e., 3–11) was carried out, and the results are displayed in Figure 7A. At pH values of 3 and 11, the findings reveal the most and least *HA* degradation efficiency levels, respectively, which are to be expected. The reasons for these results are that in a homogeneous photocatalytic degradation reactor, two eminent oxidizing species are present: the hydroxyl radical: (•OH) and positive electronic holes: (h<sup>+</sup>). The high potential can easily degrade the organic pollutants in the reactor. While the •OH can exist throughout the reactor randomly when it is generated in large quantities, the h<sup>+</sup> is present only on the surface of the photocatalyst. Therefore, wherever both the h<sup>+</sup> and •OH are present at the same time, the degradation efficiency will be high, and the contaminants will be removed. This simply means the photocatalyst surface attracts the negative *HA* ions onto its outer surface due to the electrostatic attraction between them, resulting in *HA* degradation through the active h<sup>+</sup>. These conditions prevail when the medium demonstrates an acidic pH (below 4.88). Simultaneously, the *HA* is eliminated by the •OH and h<sup>+</sup>, and Figure 7A

indicates that it is at a pH of 3 that the highest yield of degradation occurs. In Figure 7B, a graphical schematic representation is shown for a clearer understanding of this process. Other researchers have reported similar findings that correspond to the results of the current study [38].

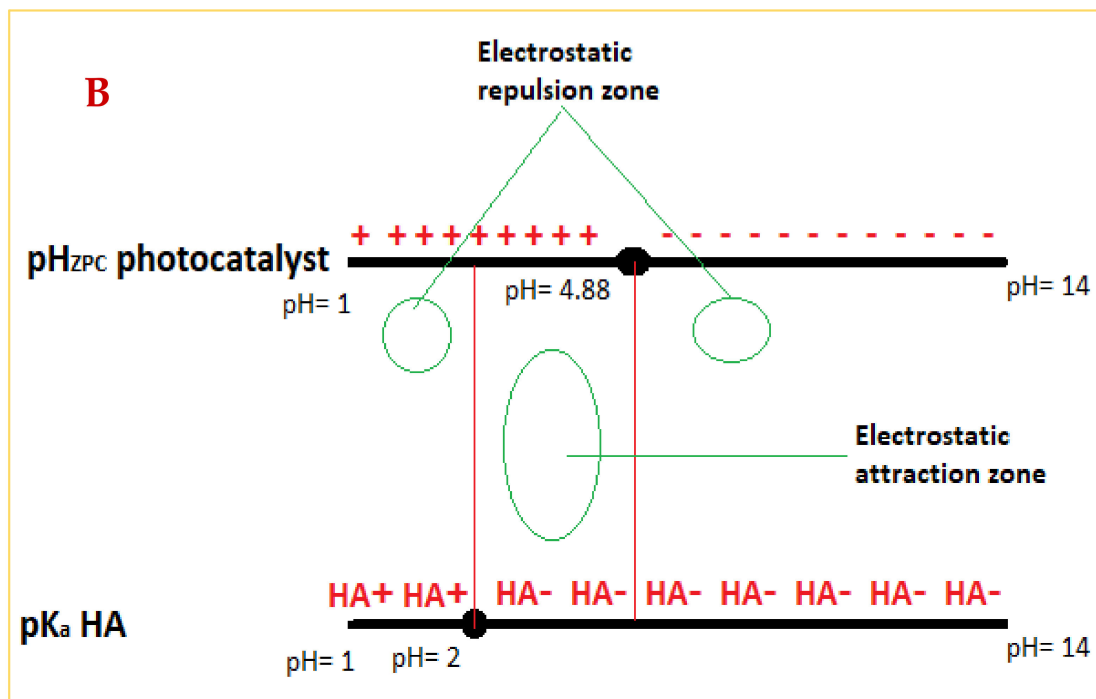
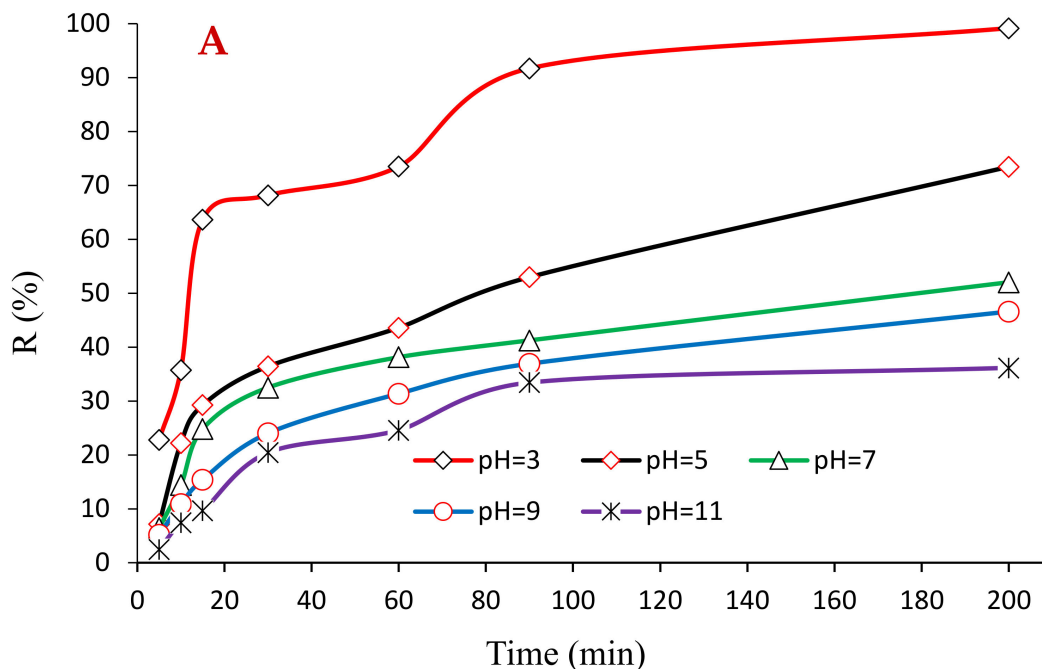


**Figure 7.** The plot of pH effect (A) and graphical schematic representation of the relationship between HA pKa and BNTN@Fe<sub>3</sub>O<sub>4</sub>@ZnO pH<sub>ZPC</sub> (B).

### 3.2.2. Influence of Photocatalyst Dose

The variable next in significance that affects the photocatalytic reaction is the dose of the photocatalyst synthesized, which influences the percent of contaminant degraded. Therefore, it is crucial to determine the optimal value of the dose for practical purposes.

To study the effect of the dose of the synthesized photocatalyst on the process of the photocatalytic degradation of HA, several doses of the bentonite@Fe<sub>3</sub>O<sub>4</sub>@ZnO magnetic nanocomposite (from 0.005 to 0.1 g/L) were experimented with under a variety of conditions (i.e., pH = 3; HA concentration = 10 mg/L; UV lamp (16-watt power)). The findings are listed in Figure 8. From this figure, the inference can be drawn that the greatest and least efficiencies were observed for the photocatalyst doses of 0.01 and 0.1 g/L, respectively. Initially, the efficiency escalated when the dose was increased from 0.005 to 0.01 g/L; however, any further increase in the dosage exceeding 0.01 g/L caused the efficiency to drop, so the lowest efficiency was observed at the highest dose of 0.1 g/L.

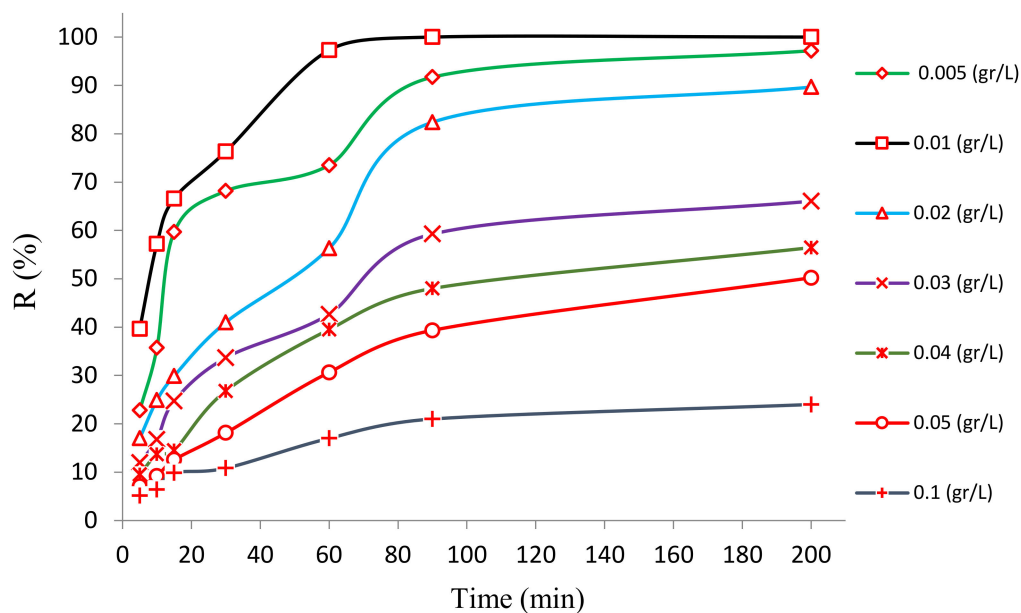


Figure 8. The plot of BNTN@Fe<sub>3</sub>O<sub>4</sub>@ZnO magnetic nanocomposite dose.

This trend is justified by the reasoning that any increase in the dose of the nanocomposite will result in the provision of a greater surface area of the photocatalyst for the absorption of UV radiation which, in turn, will generate active h<sup>+</sup> and free radicals, •OH in particular. Consequently, greater HA degradation was achieved. However, when the photocatalyst dose is increased excessively, it results in a reduction in the efficiency of the HA degradation. This is likely due to the agglomeration of the nanocomposite in which the density and the dose of the catalyst are increased, causing them to stick to one another. Similar results have been obtained in the photocatalytic elimination of contaminants through the use of magnetic nanocomposites. This occurs because the magnetic property of the nanocomposite enables them to accumulate in high doses, resulting in a reduction in UV absorption and photocatalytic action [39].

### 3.2.3. Influence of HA Concentration

Another variable that influences the photocatalytic degradation of organic contaminants is the concentration of the pollutant present in the aqueous solution [40]. From the photocatalytic reactions, it is evident that greater removal efficiency is achieved when the concentration of the contaminant is reduced. However, determining the maximum concentration that can be completely removed is proving to be a major problem. Therefore, the removal of HA through photocatalysis was investigated at different concentrations of HA (i.e., 2, 5, 10, and 15 mg/L), and the results are revealed in Figure 9. According to the results, the photocatalytic process using BNTN@Fe<sub>3</sub>O<sub>4</sub>@ZnO demonstrated the ability to completely degrade the HA when it was present in concentrations of 2, 5, and 10 mg/L within 30, 60, and 70 min, respectively; however, at a concentration of 15 mg/L, approximately 7% of the humic acid was still present in the reactor even after 200 min of contact

time during photocatalysis. The improvement in the degradation of HA is attributed to the reduction in its initial concentration. This is because under identical conditions (i.e., pH, BNTN@Fe<sub>3</sub>O<sub>4</sub>@ZnO dose, and reaction time), the elimination of HA by the •OH increases when its value is lower. Further, at a higher dose of HA, the photocatalyst surface area available for the UV absorption and the occurrence of photocatalytic actions are decreased because of the greater adhesion of the HA to the BNTN@Fe<sub>3</sub>O<sub>4</sub>@ZnO surface sites.

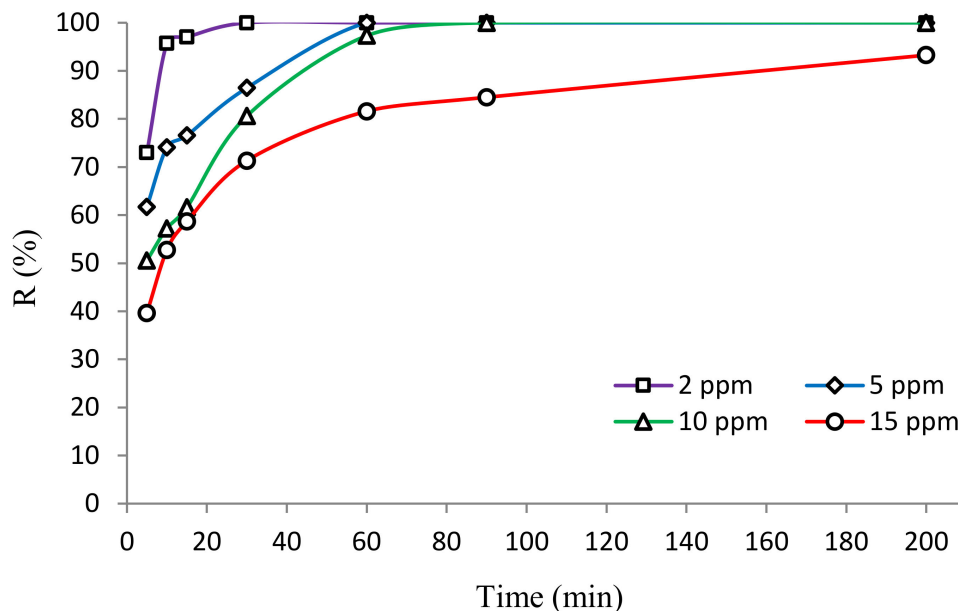


Figure 9. The plot of HA concentration levels.

### 3.2.4. Kinetics of HA Degradation

While modeling empirical data in advanced oxidation processes such as photocatalysis, the rate of organic substance oxidation must be studied, and the performance of the photocatalyst must be ascertained [41]. In the photocatalytic unit using the BNTN@Fe<sub>3</sub>O<sub>4</sub>@ZnO magnetic nanocomposite, the kinetics of HA oxidation under UV irradiation was investigated by the first-order kinetic model (using a linear plot to determine the k and integrated rate law). In Table 2, the findings of the linear analysis and the empirical HA removal data are shown. The constant rate of the reaction kinetics,  $K_{obs}$ , is obtained by plotting the linear chart of  $\ln C/C_0$  versus time (Figure 10). In addition, to model the reaction kinetics, the equation of the integrated rate law ( $C = C_0 \times e^{-K_{obs} \times t}$ ) was applied to estimate the residual HA concentration values over time t. Then, a graph was plotted of the predicted versus experimental values, and the degree of their relationship was ascertained via the determination coefficient ( $R^2$ ) [42,43]. Finally, using the Solver plugin in Excel, the best constant value of the reaction rate was fitted, as shown in Figure 11. The results provided in Table 2 and Figure 10 reveal that the  $K_{obs}$  values decrease as the HA concentrations increase so that their values were 0.2207 and 0.0155  $\text{min}^{-1}$  at HA concentrations of 2 and 15 mg/L, respectively. This suggests that rate of HA degradation was lowered as its concentration increased.

Table 2. Kinetics data for HA degradation.

Concentration (mg/L)	Equation	$K_{obs}$ ( $\text{min}^{-1}$ )	$R^2$	$t_{1/2}$ (min)
2	$y = 0.2207x + 0.3849$	0.2207	0.9411	3.140009
5	$y = 0.0389x + 0.8563$	0.0389	0.9637	17.81491
10	$y = 0.0380x + 0.4676$	0.0538	0.9811	12.88104
15	$y = 0.0284x + 0.4211$	0.0155	0.9749	44.70968

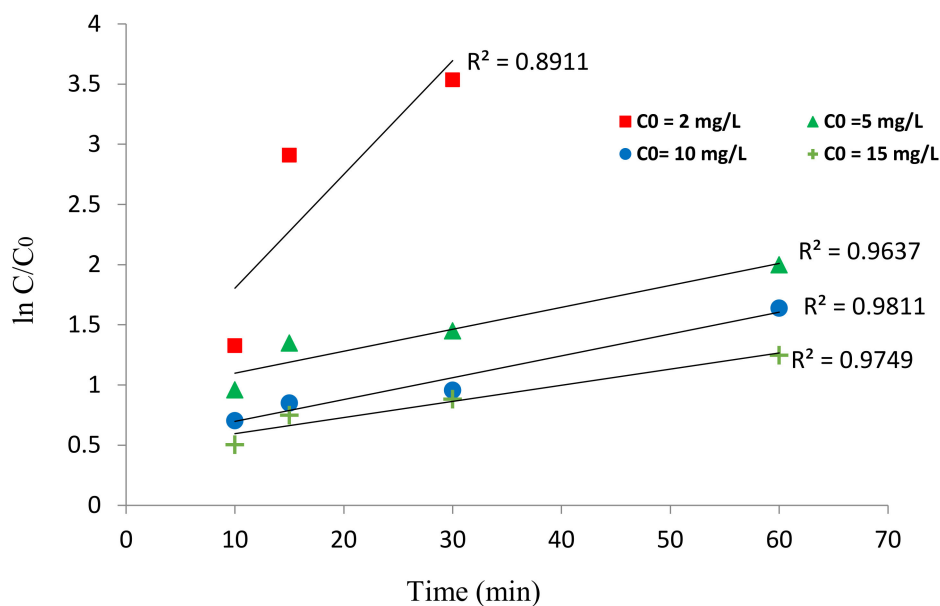


Figure 10. Linear plot of the kinetic data.

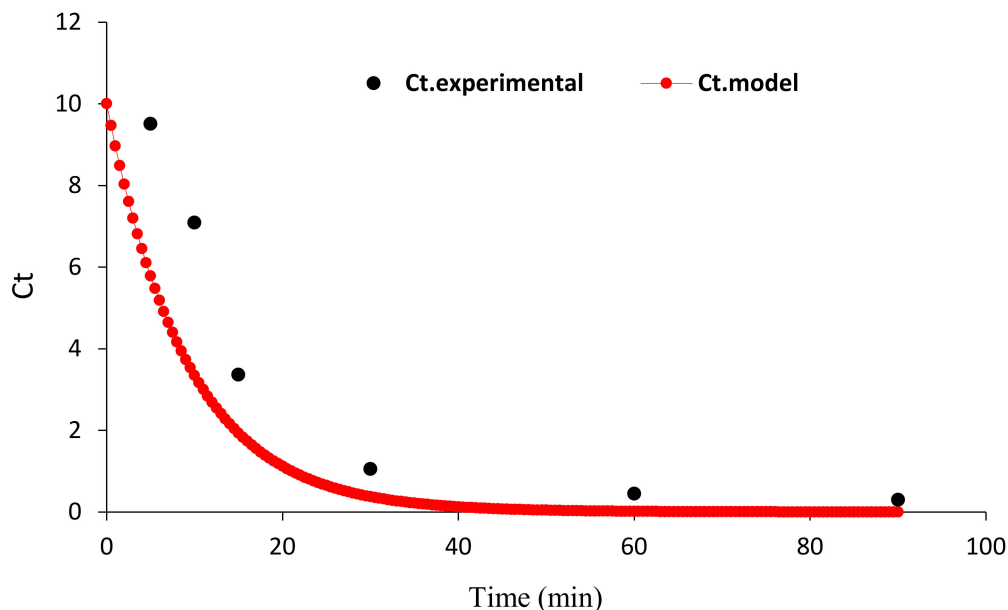


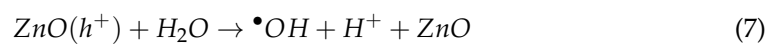
Figure 11. The plot was obtained from the Solver plugin for kinetic modeling.

As seen in Figure 11, the  $R^2$  value obtained when modeling the kinetics of HA decomposition was high (0.97), and satisfactory compliance is observed between the empirical data and the values predicted by the Langmuir–Hinshelwood model, indicating that the HA degradation data follow the first-order kinetic model.

### 3.2.5. HA Degradation Mechanism

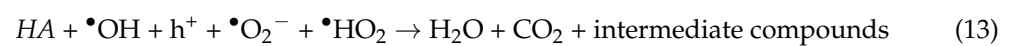
It must be noted that ZnO and TiO<sub>2</sub> are semiconductor materials with great significance as operants in photocatalysis, and no photocatalytic activity can be practically conducted without these compounds [44]. Another essential operant in the photocatalytic processes is a beam current, which is similar to UV irradiation [45]. When both of these factors are present simultaneously in the reaction chamber, the photocatalytic process will occur. The outcome of these activities is the generation of free radicals and active species in a chain of reactions through which organic substances can be easily decomposed.

The dominant property of ZnO and other semiconductors is the presence of conduction and valence bands in their configurations. These facilitate the transfer of electrons from the valence band to the conduction band by striking a beam current with their surface and creating cavities (holes:  $h^+$ ) on the surface of the photocatalyst at the same time (Equations (4)–(6)). The  $h^+$  thus created can directly degrade organic materials or decompose the water molecules and hydroxyl ions which, in turn, leads to the production of  $\bullet OH$ , known as a potent oxidant for eliminating organic pollutants (Equations (7) and (8)) [46]. Further, the electrons thus released from their orbit may react with the oxygen molecules to produce superoxide radicals ( $\bullet O_2^-$ ) (Equations (9) and (10)). The  $\bullet O_2^-$  first generates the hydroperoxyl radical ( $\bullet HO_2$ ) and then creates hydrogen peroxide ( $H_2O_2$ ) by reacting with the water molecules, and the formed  $H_2O_2$  can create  $\bullet OH$  by accepting an electron (Equations (11) and (12)). The reactions responsible are cited below:



The  $\bullet OH$  thus formed has a high redox potential to attack the *HA* compounds present and break them down into simple molecules such as water and carbon dioxide [47].

Under the optimal conditions obtained, the photocatalysis process using the BNTN@Fe<sub>3</sub>O<sub>4</sub>@ZnO magnetic nanocomposite was able to completely decompose 10 mg/L of *HA* after exposure to UV light for 90 min. Thus, it is anticipated that all *HA* molecules will be converted into water and carbon dioxide molecules, as well as some likely byproducts (intermediate compounds). The mineralization reaction occurring during photocatalysis and the general reactions are shown below (Equation (13)).



An intermediate compound that could be generated in the process of *HA* degradation through photocatalysis can be identified using gas chromatography–mass spectrometry (GC). To accomplish this, a GC device was employed to identify all the likely intermediate compounds which can be generated during the photocatalysis process. In Figure 12, the results of the GC analysis are listed. This indicates that 2-(4-nitrophenyl)-1, 3-dioxolane; methyl 3-(hydroxymethyl)-5-methyl-1, 2-oxazole-4-carboxylate; 2-(methylamino methyl) prop-2-enoate; 2-methylamino methyl-1, 3-dioxolane; 2, 2-Dimethyl-1, 3-dioxolane 2-methyl-1-butanol, and 2-methyl-1-butanol compounds are released when the *HA* is degraded during the photocatalysis process. As is evident from the chemical structure of the byproducts, all the compounds, barring 2-(4-nitrophenyl)-1 and 3-dioxolane, lack the

presence of a benzene ring. This implies that the intermediates produced have a simple structure and are biodegradable.

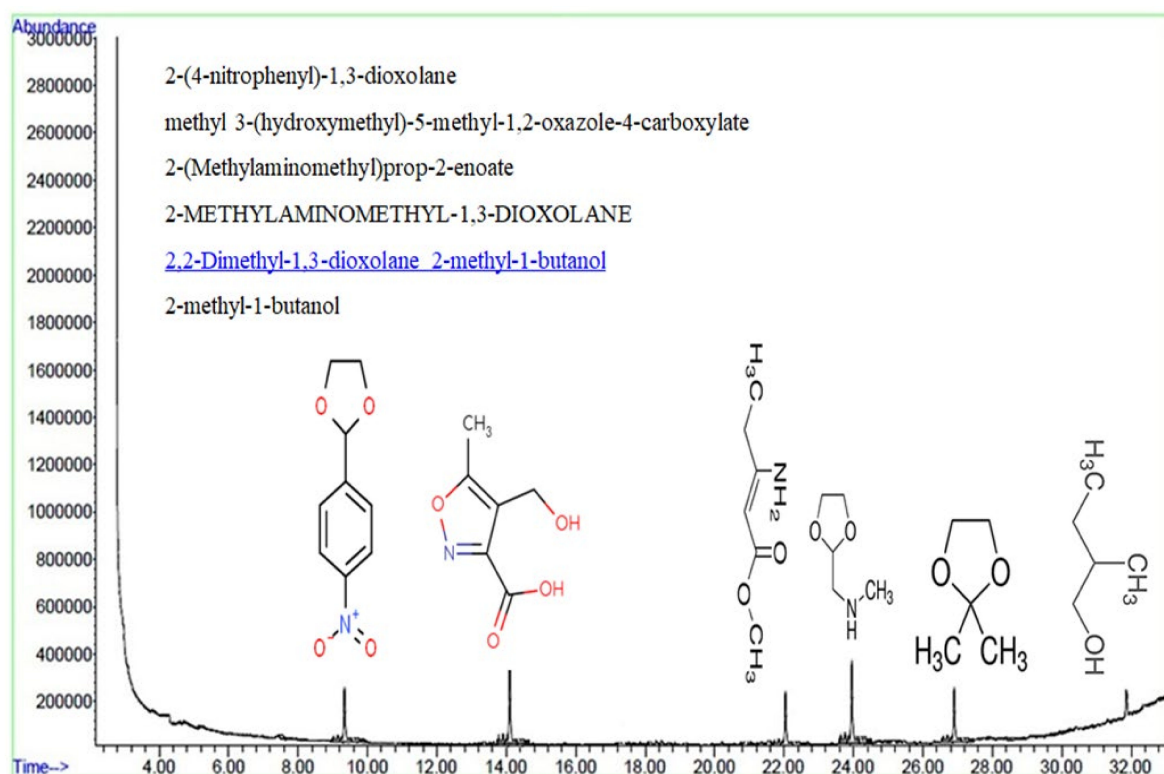


Figure 12. The results of GC analysis.

### 3.2.6. Reusability of BNTN@Fe<sub>3</sub>O<sub>4</sub>@ZnO

From Figure 13, the reusability results of the photocatalyst are evident. As observed from the corresponding figure, after four consecutive reactions, only 6% of the degradation rate was reduced. This indicates the effective reusability of the nanoparticles.

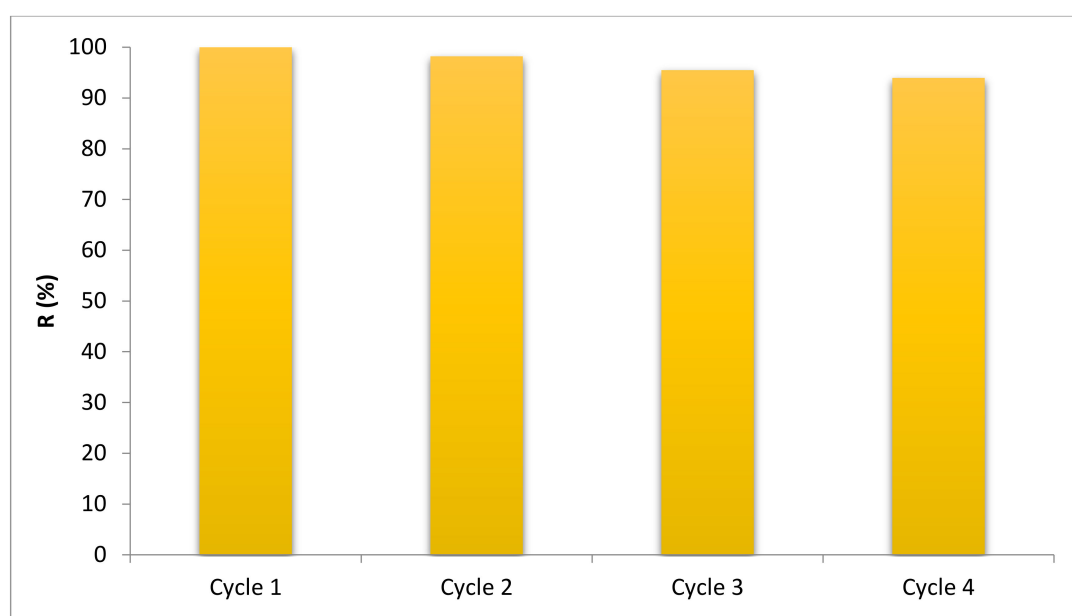


Figure 13. The reusability of the BNTN@Fe<sub>3</sub>O<sub>4</sub>@ZnO magnetic nanocomposite.

#### 4. Conclusions

In the present investigation, the sol–gel method was used to synthesize a BNTN@Fe<sub>3</sub>O<sub>4</sub>@ZnO magnetic nanocomposite. After synthesis, the characterization of this nanocomposite was carried out using FE-SEM, FT-IR, XRD, VSM, and DRS techniques. The photocatalytic properties and degradation efficiency of the magnetic nanocomposite were examined under different environmental conditions for the elimination of HA from an aqueous solution. The outcomes of the characterization study revealed that this nanocomposite had excellent morphology, suitable photocatalytic properties, a particle diameter in the nanosize range, remarkable crystallization, and strong magnetic properties. The results of the photocatalysis showed that total HA degradation was obtained under the optimal conditions, which included a pH level of 3, a nanocomposite dose of 0.01 g/L, and a concentration of HA of 10 mg/L within a reaction time of 90 min. Further, the kinetic study showed that the experimental data of the elimination of HA in aquatic systems can be modeled by applying a simplified form of the Langmuir–Hinshelwood equation. The results of the kinetic study revealed satisfactory compliance between the empirical data and the values predicted by the Langmuir–Hinshelwood model, indicating that the data acquired followed the first-order kinetic model. According to the findings of this work, the photocatalytic treatment process using BNTN@Fe<sub>3</sub>O<sub>4</sub>@ZnO magnetic nanocomposite has significant potential for the removal of humic acid compounds from aqueous solutions. As this treatment process eventually produces low-toxicity biodegradable compounds, it is proposed that this process can be used as a pretreatment process before the biological treatment of industrial or municipal wastewater.

**Author Contributions:** N.N., Conceptualization, Data curation, Investigation, Methodology, Project administration, Validation, Writing—review & editing, Resources; T.J.A.-M., Writing—review & editing, Writing—original draft, Formal analysis; A.H.P. Formal analysis, Writing—original draft; M.M., Writing—original draft; S.F.T.F., Methodology. All authors have read and agreed to the published version of the manuscript.

**Funding:** Birjand University of Medical Sciences has provided financial support for this research.

**Data Availability Statement:** Not applicable.

**Acknowledgments:** The authors express their sincere thanks to Birjand University of Medical Sciences for the support extended for the production of this paper as a University-approved project (ID project: 5927). The Ethics Committee of Birjand University of Medical Sciences (Iran) approved the study with the ethical code IR.BUMS.REC.1401.154.

**Conflicts of Interest:** The authors declare no conflict of interest.

#### References

1. Guo, Z.; Zhan, R.; Shi, Y.; Zhu, D.; Pan, J.; Yang, C.; Wang, Y.; Wang, J. Innovative and green utilization of zinc-bearing dust by hydrogen reduction: Recovery of zinc and lead, and synergetic preparation of Fe/C micro-electrolysis materials. *Chem. Eng. J.* **2023**, *456*, 141157. [[CrossRef](#)]
2. Foroutan, R.; Peighambaroust, S.J.; Amarzadeh, M.; Korri, A.K.; Peighambaroust, N.S.; Ahmad, A.; Ramavandi, B. Nickel ions abatement from aqueous solutions and shipbuilding industry wastewater using ZIF-8-chicken beak hydroxyapatite. *J. Mol. Liq.* **2022**, *356*, 119003. [[CrossRef](#)]
3. Qin, Z.; Jin, J.; Liu, L.; Zhang, Y.; Du, Y.; Yang, Y. Reuse of soil-like material solidified by a biomass fly ash-based binder as engineering backfill material and its performance evaluation. *J. Clean. Prod.* **2023**, *402*, 136824. [[CrossRef](#)]
4. Cao, T.-T.; Tie-Fu, X.; Zhao, M.-N.; Xu, J.; Cui, C.-W. Application of vacuum-ultraviolet (VUV) for phenolic homologues removal in humic acid solution: Efficiency, pathway and DFT calculation. *J. Hazard. Mater.* **2020**, *384*, 121464. [[CrossRef](#)]
5. Zhan, Y.; Zhu, Z.; Lin, J.; Qiu, Y.; Zhao, J. Removal of humic acid from aqueous solution by cetylpyridinium bromide modified zeolite. *J. Environ. Sci.* **2010**, *22*, 1327–1334. [[CrossRef](#)]
6. Wang, T.; Qu, G.; Ren, J.; Yan, Q.; Sun, Q.; Liang, D.; Hu, S. Evaluation of the potentials of humic acid removal in water by gas phase surface discharge plasma. *Water Res.* **2016**, *89*, 28–38. [[CrossRef](#)] [[PubMed](#)]
7. Wang, L.; Han, C.; Nadagouda, M.N.; Dionysiou, D.D. An innovative zinc oxide-coated zeolite adsorbent for removal of humic acid. *J. Hazard. Mater.* **2016**, *313*, 283–290. [[CrossRef](#)]
8. Tahmasebi, F.; Alimohammadi, M.; Nabizadeh, R.; Khoobi, M.; Karimian, K.; Zarei, A. Performance evaluation of graphene oxide coated on cotton fibers in removal of humic acid from aquatic solutions. *Korean J. Chem. Eng.* **2019**, *36*, 894–902. [[CrossRef](#)]

9. Zhou, X.; Zhou, S.; Ma, F.; Xu, Y. Synergistic effects and kinetics of rGO-modified TiO<sub>2</sub> nanocomposite on adsorption and photocatalytic degradation of humic acid. *J. Environ. Manag.* **2019**, *235*, 293–302. [[CrossRef](#)]
10. Ahmad, A.L.; Pang, W.Y.; Shafie, Z.M.H.M.; Zaulkiflee, N.D. PES/PVP/TiO<sub>2</sub> mixed matrix hollow fiber membrane with antifouling properties for humic acid removal. *J. Water Process Eng.* **2019**, *31*, 100827. [[CrossRef](#)]
11. Zghal, S.; Jedidi, I.; Cretin, M.; Cerneaux, S.; Abdelmouleh, M. One-step synthesis of highly porous carbon graphite/carbon nanotubes composite by in-situ growth of carbon nanotubes for the removal of humic acid and copper (II) from wastewater. *Diam. Relat. Mater.* **2020**, *101*, 107557. [[CrossRef](#)]
12. Lin, Q.; Dong, F.; Li, C.; Cui, J. Disinfection byproduct formation from algal organic matters after ozonation or ozone combined with activated carbon treatment with subsequent chlorination. *J. Environ. Sci.* **2021**, *104*, 233–241. [[CrossRef](#)]
13. Qin, J.J.; Oo, M.H.; Kekre, K.A.; Knops, F.; Miller, P. Impact of coagulation pH on enhanced removal of natural organic matter in treatment of reservoir water. *Sep. Purif. Technol.* **2006**, *49*, 295–298. [[CrossRef](#)]
14. Eskandarinezhad, S.; Khosravi, R.K.R.; Amarzadeh, M.; Mondal, P.; Filho, F.J.C.M. Application of different Nanocatalysts in industrial effluent treatment: A review. *J. Compos. Compd.* **2021**, *2*, 43–56. [[CrossRef](#)]
15. Liu, W.; Huang, F.; Liao, Y.; Zhang, J.; Ren, G.; Zhuang, Z.; Zhen, J.; Lin, Z.; Wang, C. Treatment of Cr<sup>VI</sup>-Containing Mg(OH)<sub>2</sub> Nanowaste. *Angew. Chem. Int. Ed.* **2008**, *47*, 5619–5622. [[CrossRef](#)]
16. Gonçalves, N.P.; Minella, M.; Fabbri, D.; Calza, P.; Malitesta, C.; Mazzotta, E.; Prevot, A.B. Humic acid coated magnetic particles as highly efficient heterogeneous photo-Fenton materials for wastewater treatments. *Chem. Eng. J.* **2020**, *390*, 124619. [[CrossRef](#)]
17. Geng, N.; Chen, W.; Xu, H.; Lin, T.; Ding, M.; Wang, Y.; Tao, H.; Hu, K. Preparation of Fe<sub>3</sub>O<sub>4</sub>/TiO<sub>2</sub>-N-GO sonocatalyst and using for humic acid removal with the assist of ultrasound. *Mater. Sci. Semicond. Process.* **2019**, *102*, 104593. [[CrossRef](#)]
18. Menya, E.; Olupot, P.W.; Storz, H.; Lubwama, M.; Kiros, Y. Synthesis and evaluation of activated carbon from rice husks for removal of humic acid from water. *Biomass Convers. Biorefinery* **2022**, *12*, 3229–3248. [[CrossRef](#)]
19. Li, S.; Li, Z.; Ke, B.; He, Z.; Cui, Y.; Pan, Z.; Li, D.; Huang, S.; Lai, C.; Su, J. Magnetic multi-walled carbon nanotubes modified with polyaluminium chloride for removal of humic acid from aqueous solution. *J. Mol. Liq.* **2019**, *279*, 241–250. [[CrossRef](#)]
20. Liu, J.; Chen, C.; Zhang, K.; Zhang, L. Applications of metal–organic framework composites in CO<sub>2</sub> capture and conversion. *Chin. Chem. Lett.* **2021**, *32*, 649–659. [[CrossRef](#)]
21. Ghanbari, F.; Yaghoot-Nezhad, A.; Waclawek, S.; Lin, K.Y.A.; Rodríguez-Chueca, J.; Mehdipour, F. Comparative investigation of acetaminophen degradation in aqueous solution by UV/Chlorine and UV/H<sub>2</sub>O<sub>2</sub> processes: Kinetics and toxicity assessment, process feasibility and products identification. *Chemosphere* **2021**, *285*, 131455. [[CrossRef](#)] [[PubMed](#)]
22. Guo, W.; Luo, H.; Jiang, Z.; Fang, D.; Chi, J.; Shangguan, W.; Wang, Z.; Wang, L.; Lee, A.F. Ge-Doped Cobalt Oxide for Electrocatalytic and Photocatalytic Water Splitting. *ACS Catal.* **2022**, *12*, 12000–12013. [[CrossRef](#)]
23. Huang, Z.; Ding, J.; Yang, X.; Liu, H.; Song, P.; Guo, Y.; Guo, Y.; Wang, L.; Zhan, W. Highly Efficient Oxidation of Propane at Low Temperature over a Pt- Based Catalyst by Optimization Support. *Environ. Sci. Technol.* **2022**, *56*, 17278–17287. [[CrossRef](#)]
24. Shi, Y.; Huang, J.; Zeng, G.; Cheng, W.; Yu, H.; Gu, Y.; Shi, L.; Yi, K. Stable, metal-free, visible-light-driven photocatalyst for efficient removal of pollutants: Mechanism of action. *J. Colloid Interface Sci.* **2018**, *531*, 433–443. [[CrossRef](#)] [[PubMed](#)]
25. Xin, Z.; Zhao, X.; Ji, H.; Ma, T.; Li, H.; Zhong, S.; Shen, Z. Amorphous carbon-linked TiO<sub>2</sub>/carbon nanotube film composite with enhanced photocatalytic performance: The effect of interface contact and hydrophilicity. *Chin. Chem. Lett.* **2021**, *32*, 2151–2154. [[CrossRef](#)]
26. Peleyeju, M.G.; Viljoen, E.L. WO<sub>3</sub>-based catalysts for photocatalytic and photoelectrocatalytic removal of organic pollutants from water—A review. *J. Water Process Eng.* **2021**, *40*, 101930. [[CrossRef](#)]
27. Shi, L.; Ren, Z.; Zhou, C.; Shen, L.; Bai, H. Numerical simulation of an entangled wire-silicone rubber continuous interpenetration structure based on domain meshing superposition method. *Compos. Part B* **2023**, *256*, 110648. [[CrossRef](#)]
28. Zhang, X.; Ma, F.; Dai, Z.; Wang, J.; Chen, L.; Ling, H.; Soltanian, M.R. Radionuclide transport in multi-scale fractured rocks: A review. *J. Hazard. Mater.* **2022**, *424*, 127550. [[CrossRef](#)]
29. Tang, X.; Tang, R.; Xiong, S.; Zheng, J.; Li, L.; Zhou, Z.; Gong, D.; Deng, Y.; Su, L.; Liao, C. Application of natural minerals in photocatalytic degradation of organic pollutants: A review. *Sci. Total Environ.* **2022**, *812*, 152434. [[CrossRef](#)]
30. Zheng, R.; Gao, H.; Ren, Z.; Cen, D.; Chen, Z. Preparation of activated bentonite and its adsorption behavior on oil-soluble green pigment. *Physicochem. Probl. Miner. Process.* **2017**, *53*, 829–845. [[CrossRef](#)]
31. Patehkor, H.A.; Fattahi, M.; Khosravi-Nikou, M. Synthesis and characterization of ternary chitosan–TiO<sub>2</sub>–ZnO over graphene for photocatalytic degradation of tetracycline from pharmaceutical wastewater. *Sci. Rep.* **2021**, *11*, 1–17. [[CrossRef](#)]
32. Tobajas, M.; Belver, C.; Rodriguez, J.J. Degradation of emerging pollutants in water under solar irradiation using novel TiO<sub>2</sub>-ZnO/clay nanoarchitectures. *Chem. Eng. J.* **2017**, *309*, 596–606. [[CrossRef](#)]
33. Foroutan, R.; Peighambaroust, S.J.; Latifi, P.; Ahmadi, A.; Alizadeh, M.; Ramavandi, B. Carbon nanotubes/β-cyclodextrin/MnFe<sub>2</sub>O<sub>4</sub> as a magnetic nanocomposite powder for tetracycline antibiotic decontamination from different aqueous environments. *J. Environ. Chem. Eng.* **2021**, *9*, 106344. [[CrossRef](#)]
34. Xu, R.; Wang, Y.-N.; Sun, Y.; Wang, H.; Gao, Y.; Li, S.; Guo, L.; Gao, L. Ecotoxicology and Environmental Safety External sodium acetate improved Cr (VI) stabilization in a Cr-spiked soil during chemical-microbial reduction processes: Insights into Cr (VI) reduction performance, microbial community and metabolic functions. *Ecotoxicol. Environ. Saf.* **2023**, *251*, 114566. [[CrossRef](#)] [[PubMed](#)]

35. Aragaw, T.A.; Bogale, F.M.; Aragaw, B.A. Iron-based nanoparticles in wastewater treatment: A review on synthesis methods, applications, and removal mechanisms. *J. Saudi Chem. Soc.* **2021**, *25*, 101280. [[CrossRef](#)]
36. Norabadi, E.; Panahi, A.H.; Ghanbari, R.; Meshkinian, A.; Kamani, H.; Ashrafi, S.D. Optimizing the parameters of amoxicillin removal in a photocatalysis/ozonation process using Box–Behnken response surface methodology. *Desalin. Water Treat.* **2020**, *192*, 234–240. [[CrossRef](#)]
37. Dai, Z.; Ma, Z.; Zhang, X.; Chen, J.; Ershadnia, R.; Luan, X.; Soltanian, M.R. An integrated experimental design framework for optimizing solute transport monitoring locations in heterogeneous sedimentary media. *J. Hydrol.* **2022**, *614*, 128541. [[CrossRef](#)]
38. Birben, N.C.; Paganini, M.C.; Calza, P.; Bekbolet, M. Photocatalytic degradation of humic acid using a novel photocatalyst: Ce-doped ZnO. *Photochem. Photobiol. Sci.* **2017**, *16*, 24–30. [[CrossRef](#)]
39. Khodadadi, M.; Al-Musawi, T.J.; Kamani, H.; Silva, M.F.; Panahi, A.H. The practical utility of the synthesis FeNi<sub>3</sub>@SiO<sub>2</sub>@TiO<sub>2</sub> magnetic nanoparticles as an efficient photocatalyst for the humic acid degradation. *Chemosphere* **2020**, *239*, 124723. [[CrossRef](#)]
40. Yaghoot-Nezhad, A.; Saebnoori, E.; Danaee, I.; Elahi, S.; Panah, N.B.; Khosravi-Nikou, M.R. Evaluation of the oxidative degradation of aromatic dyes by synthesized nano ferrate(VI) as a simple and effective treatment method. *J. Water Process Eng.* **2022**, *49*, 103017. [[CrossRef](#)]
41. Yaghoot-Nezhad, A.; Moradi, M.; Rostami, M.; Danaee, I.; Khosravi-Nikou, M.R. Dual Z-Scheme CuO-ZnO@Graphitic Carbon Nitride Ternary Nanocomposite with Improved Visible Light-Induced Catalytic Activity for Ultrasound-Assisted Photocatalytic Desulfurization. *Energy Fuels* **2020**, *34*, 13588–13605. [[CrossRef](#)]
42. Kavurmaci, S.S.; Bekbolet, M. Photocatalytic degradation of humic acid in the presence of montmorillonite. *Appl. Clay Sci.* **2013**, *75–76*, 60–66. [[CrossRef](#)]
43. Li, X.; Yu, P.; Niu, X.; Yamaguchi, H.; Li, D. Non-contact manipulation of nonmagnetic materials by using a uniform magnetic field: Experiment and simulation. *J. Magn. Magn. Mater.* **2019**, *497*, 165957. [[CrossRef](#)]
44. Wang, T.; Zhou, J.; Wang, W.; Zhu, Y.; Niu, J. Ag-single atoms modified S1.66-N1.91/TiO<sub>2</sub>-x for photocatalytic activation of peroxymonosulfate for bisphenol A degradation. *Chin. Chem. Lett.* **2022**, *33*, 2121–2124. [[CrossRef](#)]
45. Li, F.; Wang, L.; Qu, G.; Hou, P.; Kong, L.; Huang, J.; Xu, X. An integrated approach to configure rGO/VS<sub>4</sub>/S composites with improved catalysis of polysulfides for advanced lithium–sulfur batteries. *Chin. Chem. Lett.* **2022**, *33*, 3909–3915. [[CrossRef](#)]
46. Feng, C.; Lu, Z.; Zhang, Y.; Liang, Q.; Zhou, M.; Li, X.; Yao, C.; Li, Z.; Xu, S. A magnetically recyclable dual Z-scheme GCNQDs-CoTiO<sub>3</sub>/CoFe<sub>2</sub>O<sub>4</sub> composite photocatalyst for efficient photocatalytic degradation of oxytetracycline. *Chem. Eng. J.* **2022**, *435*, 134833. [[CrossRef](#)]
47. Zhao, Y.; Li, Q.; Cui, Q.; Ni, S.Q. Nitrogen recovery through fermentative dissimilatory nitrate reduction to ammonium (DNRA): Carbon source comparison and metabolic pathway. *Chem. Eng. J.* **2022**, *441*, 135938. [[CrossRef](#)]

**Disclaimer/Publisher’s Note:** The statements, opinions and data contained in all publications are solely those of the individual author(s) and contributor(s) and not of MDPI and/or the editor(s). MDPI and/or the editor(s) disclaim responsibility for any injury to people or property resulting from any ideas, methods, instructions or products referred to in the content.